Impact of Spectral Resolution on SIF Quantification for Explaining Almond Yield Variability

Thulasi Vishwanath Harish [1], Tomás Poblete [1], Victoria Gonzalez-Dugo [2], John M. Fielke [3], Pablo J. Zarco-Tejada [2]

[1] School of Agriculture, Food and Ecosystem Sciences, Faculty of Science, University of Melbourne, Melbourne, VIC 3010, Australia - thulasi.vishwanathharish@student.unimelb.edu.au, tomas.pobletecisterna@unimelb.edu.au
[2] Instituto de Agricultura Sostenible (IAS), Consejo Superior de Investigaciones Científicas (CSIC), Avenida Menéndez Pidal s/n, 14004 Córdoba, Spain - victoria.gonzalez@ias.csic.es, pablo.zarco@csic.es
[3] School of Agriculture, Food and Wine, Adelaide University, Waite Campus, Urrbrae SA 5064, Australia - john.fielke@adelaide.edu.au

Keywords: Solar-induced Chlorophyll Fluorescence, Hyperspectral Imagery, Spectral resolution, Almond Yield.

Abstract

Spatial variability in almond yield reflects complex interactions between canopy structure, physiological status, and environmental conditions. Reliable, objective yield characterization is essential for precision orchard management. Remote sensing offers a data-driven alternative to traditional assessments, with recent advances highlighting the potential to better understand yield variability through solar-induced chlorophyll fluorescence (SIF) as a direct proxy of photosynthetic activity. This study evaluates the contribution of SIF, quantified at different spectral resolutions, to explaining yield variability in a commercial almond orchard in South Australia. Airborne hyperspectral data was acquired to retrieve SIF at different resolutions and wavelengths and to retrieve structural and biochemical canopy traits. In addition, thermal images were used to retrieve the Crop Water Stress Index (CWSI). These variables were analysed using a Gaussian Process Regression (GPR) model to assess how spectral resolution and the wavelength selection used for SIF quantification influence the ability to track variability in almond yield. Results demonstrate that SIF derived from high-resolution (0.1 nm FWHM) imagery significantly improves yield-variability estimates compared to mid-resolution imagery (5.8 nm FWHM). SIF quantified in the O_2A absorption band (~ 760 nm) contributed more strongly than O_2B (~ 687 nm), while the inclusion of O_2B provided only marginal additional benefit. These findings highlight the importance of spectral resolution for exploiting SIF in precision orchard management.

1. Introduction

Assessing the spatial variability of almond yield in commercial orchards is a valuable tool for growers, providing insights into crop productivity to optimize economic returns. However, crop yield is influenced by multiple site-specific factors, including orchard architecture, canopy structure, environmental conditions, soil properties, irrigation, and agronomic management. Traditionally, experienced estimators survey almond orchards before harvest to provide early-season yield estimates, often incorporating historical yield data. However, these estimates are prone to bias and lack objectivity. Alternatively, remote sensing data is increasingly used to provide a more reliable, data-driven foundation for almond yield estimation, offering objective and scientifically validated insights. In previous studies, Gonzalez-Dugo *et al.* (2019) used thermal imagery to assess yield variability induced by imposed water stress. In another study, Tang *et al.* (2023) used multispectral imagery, and the red-edge region was found to be sensitive to variability in almond yield. One of the most recent advances in high-resolution imaging spectroscopy focuses on quantifying radiation inside very narrow telluric absorption bands within the solar spectrum. These bands are caused by the strong absorption of light by atmospheric elements at specific spectral wavelengths, also known as Fraunhofer lines (FL). These narrow absorption bands can be used to quantify solar-induced chlorophyll fluorescence (SIF), the re-emitted radiation from chlorophyll molecules at longer wavelengths, modulated by photosynthesis. SIF derived from the oxygen absorption features centred near 760 nm and 687 nm is termed as SIF-O_2A and SIF-O_2B, respectively.

SIF is one of the most direct proxies of photosynthesis that can be derived from remote sensing data. SIF, along with other standard indicators of crop physiological status, such as chlorophyll a+b (Cab), carotenoids (Car), and structural traits such as leaf area index (LAI), have been shown to be useful for describing the observed variability in almond orchards linked to nutrients (Wang *et al.,* 2022). Nevertheless, most work in precision agriculture is carried out with standard hyperspectral sensors that acquire imagery at mid-resolution, i.e., with a FWHM of around 5 nm. However, many FLs, such as SIF-O_2B, cannot be quantified using mid-resolution imagery due to the narrow width and shallow depth of the absorption features (Belwalkar *et al.,* 2022). In high-resolution imagery with FWHM < 1 nm, these absorption features are more clearly distinguishable (Figure 2).

This study investigates the potential of SIF, retrieved from airborne hyperspectral imagery at high (0.1 nm FWHM) and mid (5.8 nm FWHM) spectral resolutions, to explain yield variability in almond orchards. SIF derived from the O_2A and O_2B absorption features are integrated with physiological and structural traits, including the Crop Water Stress Index (CWSI), Cab, Car, and LAI. The analysis examines the influence of spectral resolution on SIF performance, evaluates the added value of incorporating the O_2B band alongside O_2A, and assesses the relative contributions of each absorption feature to yield variability.

2. Study Area and Data

2.1 Study Area

The study area is a 120-hectare commercial almond orchard located in the Murtho region, northeast of Renmark, South Australia (Figure 1). The orchard was established in two phases in 2016 and 2018 and includes the almond varieties Nonpareil, Maxima, Rhea, Mira, Vella, and Carina.

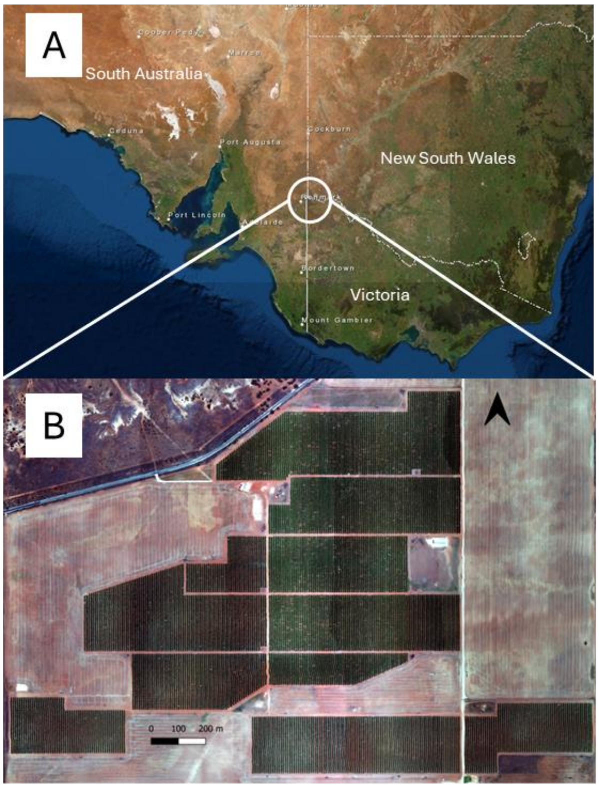

Figure 1. (A) Study area located in Murtho region, South Australia (Government of South Australia, 2026). (B) True colour airborne image of the almond orchard acquired on 11th January 2024.

2.2 Hyperspectral and Thermal Imagery

An airborne campaign was conducted on January 11th, 2024, approximately two months before harvest. Data was acquired from (i) a Hyperspec VNIR E-Series (400–1000 nm; 5.8 nm FWHM) for mid-resolution imagery; (ii) a Hyperspec Fluorescence sensor (670 - 780 nm; 0.1 - 0.2 nm FWHM) for high-resolution imagery; and (iii) a thermal infrared sensor (A655sc model, FLIR Systems, Wilsonville, OR, USA) installed on a Cessna-172 aircraft operated by the HyperSens Laboratory, University of Melbourne's Airborne Remote Sensing Facility. The hyperspectral sensors were radiometrically calibrated in the laboratory using an integration sphere (Labsphere XTH2000C, Labsphere Inc., North Sutton, NH, USA). The thermal imagery was calibrated using soil temperature as described by Calderón *et al.* (2013). The processed images were segmented to isolate sunlit vegetation pixels representing the top of the canopy by following a methodology proposed Wang *et al.* (2022). Temperature, radiance and reflectance values were extracted for analysis using QGIS plugin (Silvani, Dymaxion Labs, 2019).

In addition, ground-based irradiance measurements were acquired using a QEPRO spectrometer (Ocean Insight Inc., Dunedin, FL, USA) with a spectral resolution of 0.32 nm FWHM.

2.3 Almond Yield

Yield data were obtained from Ag-IQ Australia Almond Yield Mapper (https://www.ag-iq.com/) during the harvest period from February 29th, 2024, to April 30th, 2024. The yield mapper is based on a LiDAR sensor set up on the harvester machinery to measure the flow of almonds into the reservoir cart. It provided relative yield values used to analyse the spatial variability of yield in this study. Empirical Bayesian Kriging (EBK), a geostatistical interpolation method, was applied to the relative yield values to obtain yield maps.

3. Methodology

This section first describes the methodology used for trait quantification and then details the standardisation procedures used to spatially align the quantified traits with yield data from yield maps. Finally, it explains the approach used to assess the effectiveness of the quantified traits in explaining spatial variability in almond yield.

The methodological workflow illustrated in Figure 3 consists of three stages: (1) data preparation, including plant trait quantification and data standardization; (2) model processing; and (3) model validation.

3.1 Plant Traits Quantification

3.1.1 Crop Water Stress Index: Canopy temperature measurements were used to compute CWSI formulated by Idso *et al.* (1981), and as shown in the equation below:

$$\mathrm{CWSI}=\frac{(\mathrm{T_c}\text{-}\mathrm{T_a}) - (\mathrm{T_c}\text{-}\mathrm{T_a})_{\mathrm{LL}}}{(\mathrm{T_c}\text{-}\mathrm{T_a})_{\mathrm{UL}} - (\mathrm{T_c}\text{-}\mathrm{T_a})_{\mathrm{LL}}} \tag{1}$$

where T_c = Canopy temperature in ºC
T_a = Air temperature in ºC

Canopy temperature was derived by averaging the temperature values of sunlit vegetation pixels within the segmented tree crown from thermal imagery as illustrated in data preparation stage of Figure 3. The Non-Water-Stressed Baseline (NWSB) for mature almond orchards established by Bellvert *et al.* (2018) was applied to derive the upper $(T_c - T_a)_{UL}$ and lower $(T_c - T_a)_{LL}$ limits, corresponding to conditions of maximum potential transpiration and zero transpiration, respectively. This calculation requires air temperature and relative humidity data, which were obtained from the Murtho weather station, operated by the Landscape Weather Network in South Australia.

3.1.2 Chlorophyll, Carotenoids and Leaf Area Index: Leaf pigment and structural traits, such as Cab, Car, and LAI, were retrieved from the PRO4SAIL Radiative Transfer Model (RTM). A Look-Up Table (LUT) consisting of one million simulated reflectance spectra was generated by systematically varying leaf and canopy input parameters within predefined ranges, using a continuous uniform random numbers generator function. Leaf structure, Cab, Car, anthocyanin content, and LAI were varied within ranges of 1 - 4, 20 - 70 µg/cm^2, 3 - 20 µg/cm^2, 1 - 10 µg/cm^2, and 1 - 7 m^2/m^2, respectively, while the leaf angle distribution ranged from 10º to 90º. Dry matter content, water content, and the brown pigment content were fixed at 0.022 g/cm^2, 0.05 g/cm^2, and 0, respectively. The sun zenith angle was set to 17.34° to match the acquisition conditions.

Thereafter, the simulated reflectance from PRO4SAIL with a spectral resolution of 1 nm was subjected to Gaussian convolution spectral resampling function (Belwalkar *et al.,* 2022) to ensure spectral compatibility with mid-resolution (5.8 nm FWHM) hyperspectral imagery. Trait retrieval was performed using a Root Mean Square Error (RMSE) inversion approach, where the RMSE was computed between each measured reflectance spectrum and all simulated spectra within the LUT. The Cab, Car, and LAI values corresponding to the lowest 0.1% of RMSE values of the simulated spectra were averaged to estimate the biochemical and structural traits associated with each measured spectrum. This is illustrated in the data preparation stage in Figure 3 where the measured reflectance of a tree crown represented as red line is wrapped by light grey lines which corresponds to the lowest 0.1% of the RMSE values of the simulated spectra. The distribution of the retrieved Cab, Car and LAI is depicted in Figure 4B-D.

3.1.3 Solar Induced Chlorophyll Fluorescence: SIF is quantified using O_2A (~ 760 nm) and O_2B (~ 687 nm) oxygen absorption features. Figure 2 illustrates top-of-canopy radiance at the O_2A and O_2B absorption features acquired at different spectral resolutions, demonstrating that higher spectral resolution imagery captures finer spectral details.

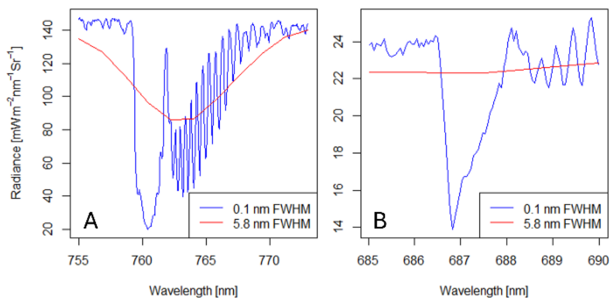

Figure 2. Top of canopy radiance spectra at (A) O_2A and (B) O_2B absorption feature acquired at 0.1 nm and 5.8 nm FWHM.

SIF is retrieved by applying the 3FLD method described by Maier *et al.* (2004) as shown in the equation below:

$$\mathrm{SIF} = \frac{(E_L * W_L + E_R * W_R) * L_{in} - (L_L * W_L + L_R * W_R) * E_{in}}{(E_L - E_{in})} \tag{2}$$

where E_L, E_R = Irradiance at the left and right shoulder of the absorption feature [$mWm^{-2}nm^{-1}$].
E_{in} = Minimum irradiance within the absorption feature [$mWm^{-2}nm^{-1}$].
L_L, L_R = Radiance at the left and right shoulder of the absorption feature [$mWm^{-2}nm^{-1}Sr^{-1}$].
L_{in} = Minimum radiance within the absorption feature [$mWm^{-2}nm^{-1}Sr^{-1}$].
W_L, W_R = Weights assigned to the left and right shoulders of the absorption feature, $W_L + W_R = 1$, corresponding to the spectral distance of the shoulders to or from the inside of the absorption feature.

To mitigate the effects of atmospheric interference, SIF calculated from non-fluorescent targets, such as bare soil, is used to correct SIF values derived from top-of-canopy radiance (Belwalkar *et al.*, 2022).

3.2 Data Standardization

Almond orchards are typically planted in alternating rows of pollinator and non-pollinator varieties, which can introduce varietal interference in tree-level analyses. To mitigate this effect during the preparation stage, a regular grid of 30 × 30 m^2 cells was generated in QGIS to provide spatial coverage of the study area, with each cell encompassing multiple tree crowns. To spatially associate tree-level traits with yield, the yield map was overlaid with the segmented tree crown layer. Yield raster pixels within each crown boundary were extracted, and their mean value was assigned as relative yield. Tree crowns were subsequently assigned to grid cells based on maximum area of overlap, and crown attributes within each grid cell were aggregated using the mean. This grid-based aggregation increased data homogeneity and reduced varietal interference by integrating multiple orchard rows within each cell. For each grid cell, relative yield was defined as the response variable, while the explanatory variables included CWSI, Cab, Car, LAI, and SIF.

3.3 Data Processing and Validation

In the processing stage, Gaussian Processes Regression (GPR) model was developed by applying the holdout cross validation method, where 70% of the data was used for training. The remaining 30% of the testing subset was applied to the trained model to generate relative yield estimates. The iterative modelling procedure was repeated up to 50 iterations to ensure robustness of the estimates, and mean estimates were derived across iterations. In the validation stage, the mean of the relative yield estimates was compared against measured relative yield values extracted from yield map to evaluate model performance using statistical metrics, including the R^2 and the derived regression equation.

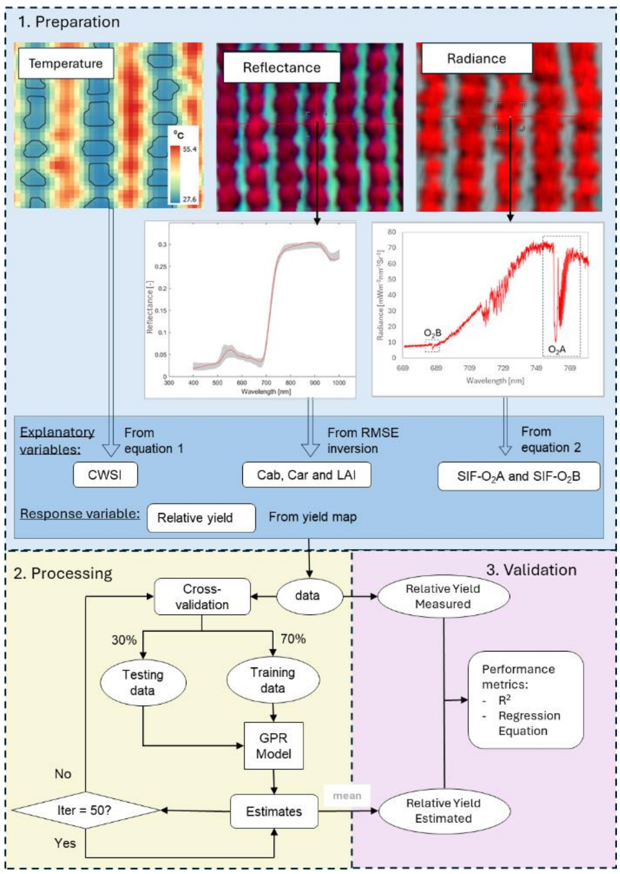

Figure 3. Overview of the methodological workflow illustrating data preparation, model processing, and validation.

Data processing and validation is implemented to three different cases to assesses the impact of SIF quantified from high- (0.1 nm FWHM) and mid-resolution (5.8 nm FWHM) airborne hyperspectral imagery on tracking yield variability in almond orchards. The three cases were evaluated by combining quantified traits including the CWSI, Cab, Car, and LAI with SIF derived from: (A) O_2A at mid-resolution and high-resolution to compare the effect of spectral resolution; (B) O_2A at mid-resolution is compared with SIF derived from O_2A + O_2B at high-resolution to evaluate the contribution of O_2B to explaining yield variability; and (C) O_2A and O_2B quantified at high-resolution is compared to assess their individual contributions to explaining yield variability.

4. Results and Discussion

4.1 Characterization of Explanatory Features

The distribution of the quantified traits, CWSI derived from thermal imagery, Cab Car and LAI retrieved through inversion of reflectance data, and SIF quantified from radiance data is illustrated in Figure 4.

As shown in Figure 4A, CWSI values range from 0.11 to 0.28, with a mean of 0.16, indicating the absence of significant water stress across the study area. These values are consistent with expectations for commercial almond orchards where irrigation management typically maintains adequate water availability. CWSI accounts for environmental variability driven by air temperature, wind speed, relative humidity and Vapour Pressure Deficit (VPD). In addition, CWSI has been reported to exhibit a strong relationship with crop transpiration and to influence almond yield (Gonzalez-Dugo *et al.,* 2019).

The retrieved leaf pigment contents show Cab values ranging from 44.71 to 64.32 μg/cm^2 and Car values ranging from 9.05 to 12.38 μg/cm^2 with mean values of 58.26 μg/cm^2 and 11.35 μg/cm^2 respectively. The retrieved LAI exhibits a mean value of 3.64 for well managed mature almond canopies. Previous studies have reported that Cab plays a significant role in estimating nitrogen concentration in almond trees (Wang *et al*., 2022). Figure 4E-F represents SIF-O_2A that was retrieved from radiance data acquired at moderate resolution (5.8 nm FWHM) imagery with values ranging from 2.89 to 11.14 mWm^{-2}nm^{-1}Sr^{-1} and at high resolution (0.1 nm FWHM) imagery with values ranging from 0.2 to 0.6 mWm^{-2}nm^{-1}Sr^{-1} respectively. While Figure 4G depicts SIF-O_2B that was retrieved only from high resolution (0.1 nm FWHM) imagery with values ranging from 0.59 to 0.71 mWm^{-2}nm^{-1}Sr^{-1} respectively. The absolute values of these ranges are consistent with the findings of Belwalkar *et al.* (2022), which report that higher spectral resolution leads to improved retrieval accuracy in the quantification of SIF.

Air temperature and VPD influences the relationship between SIF and crop productivity (Huang *et al.,* 2025). But this analysis is based on data acquired on a single acquisition date, and the environmental conditions were spatially uniform across the orchard, so this does not introduce variability into the results. Future analyses incorporating multiple observations should take into account the influence of environmental drivers, such as VPD and air temperature, on SIF and crop productivity relationships.

4.2 Impact of Spectral Resolution on SIF

Incorporating SIF has been shown to enhance the capability to monitor vegetation photosynthetic activity (Damm *et al.,* 2010). However, accurate and reliable SIF quantification critically depends on the spectral resolution of the imagery (Meroni *et al.,* 2009). As illustrated in Figure 2, the SIF-O_2A signal exhibits reduced spectral definition at mid-spectral resolution compared to high-resolution observations, while the SIF-O_2B signal becomes indistinguishable at mid-resolution. To evaluate the influence of spectral resolution and absorption features on the ability to track almond yield variability in an orchard, three cases were analysed.

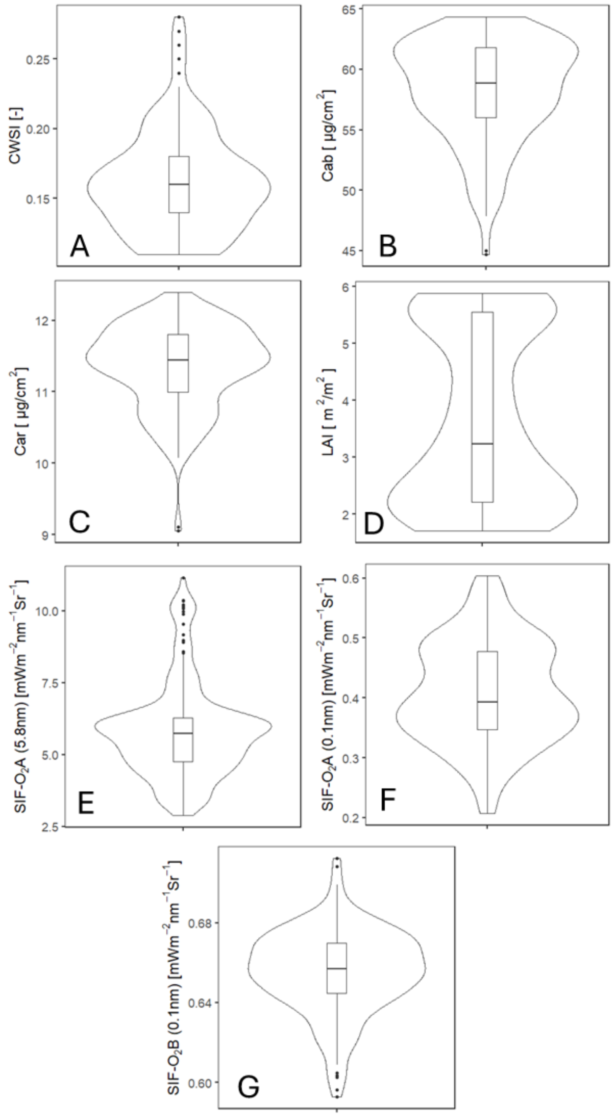

Figure 4. Distribution of the quantified traits: (A) CWSI, (B) Chlorophyll content, (C) Carotenoid content, and (D) Leaf Area Index, (E) SIF-O_2A (5.8 nm FWHM), (F) SIF-O_2A (0.1 nm FWHM), and (G) SIF-O_2B (0.1 nm FWHM) (n = 165).

In Case A, represented in Figure 5, two regression models were developed to evaluate the impact of spectral resolution on almond yield variability. Both models included CWSI, Cab, Car, and LAI as explanatory variables. The first model incorporated SIF-O_2A retrieved from 5.8 nm FWHM imagery, yielding an R^2 of 0.57. The second model substituted this with SIF-O_2A retrieved at a higher spectral resolution of 0.1 nm FWHM resulting in an increased R^2 of 0.66. The improvement in model performance demonstrates that high resolution SIF-O_2A substantially contributed to the model's ability to capture almond yield variability. This highlights the critical role of spectral resolution in accurately quantifying SIF signals, consistent with observations that SIF retrieved from mid-resolution imagery tends to overestimate fluorescence (Belwalkar *et al.,* 2024).

Expanding on these observations, Case B presented in Figure 6 examined the additional contribution of SIF-O_2B by comparing two regression models, following the same approach as in Case A. The first model comprising CWSI, Cab, Car, LAI, and SIF-O_2A retrieved from 5.8 nm FWHM imagery achieved an R^2 of 0.57, consistent with the performance observed in Case A. In the second model, high-resolution SIF-O_2A (0.1 nm FWHM) was retained and SIF-O_2B (0.1 nm FWHM) was added as an additional explanatory variable. Despite this addition, model performance improved only marginally, with R^2 increasing from 0.66 to 0.67, indicating that SIF-O_2A is the dominant contributor to tracking almond yield variability, while SIF-O_2B makes minor contributions. However, Verrelst *et al.* (2016) reported that including both SIF-O_2A and SIF-O_2B improved the accuracy of tracking photosynthetic activity.

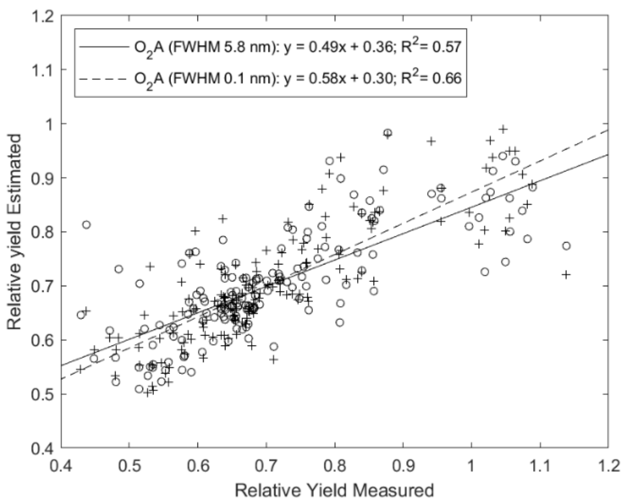

Figure 5. Relationships between the measured and estimated relative almond yield values for Case (A). 'o' indicates O_2A from 5.8 nm FWHM; '+' indicates O_2A from 0.1 nm FWHM.

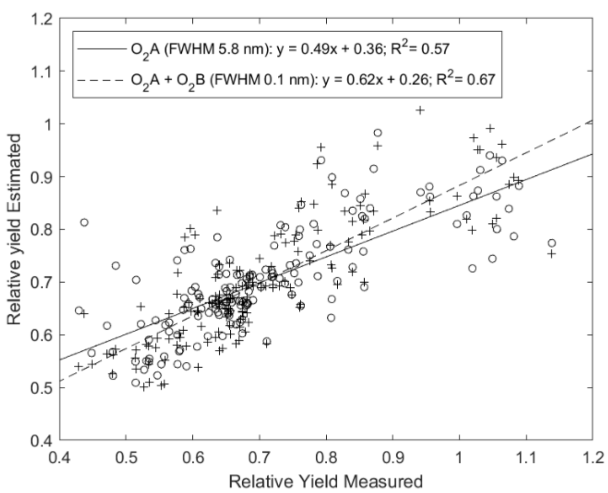

Figure 6. Relationships between the measured and estimated relative almond yield values for Case (B). 'o' indicates O_2A from 5.8 nm FWHM; '+' indicates O_2A and O_2B from 0.1 nm FWHM.

Figure 7, corresponding to Case C, further supports the observations from Case B. Following the approach used in Cases A and B, two regression models are developed, with CWSI, Cab, Car, and LAI as explanatory variables. The first model, incorporating SIF-O_2A retrieved from 0.1 nm FWHM, achieved an R^2 of 0.66, while the second model which included SIF-O_2B retrieved from 0.1 nm FWHM yielded an R^2 of 0.52. These results demonstrate that high-resolution SIF-O_2A consistently outperforms high-resolution SIF-O_2B in explaining almond yield variability. SIF-O_2B is mainly attributed to fluorescence emission of Photosystem II, and SIF-O_2A is attributed to Photosystem I (PS I) and Photosystem II (PSII) (Baker, 2008). This provides more insights into the analysis, indicating the importance of both PSI and PSII in tracking yield variability.

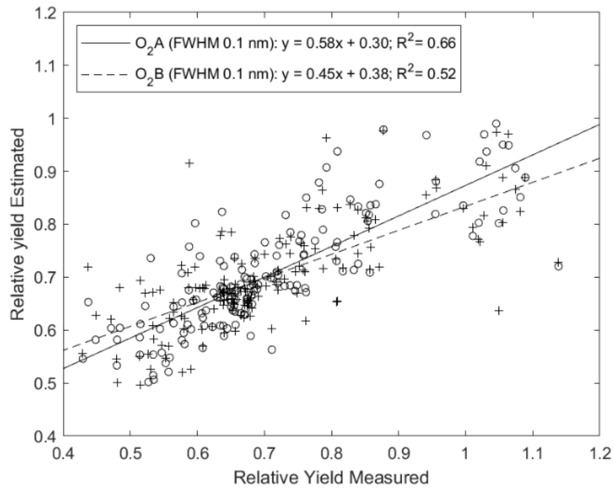

Figure 7. Relationships between the measured and estimated relative almond yield values for Case (C). 'o' indicates O_2A from 0.1 nm FWHM; '+' indicates O_2B from 0.1 nm FWHM.

5. Conclusions

This study investigated the potential of SIF for monitoring almond yield variability at the orchard scale. Results demonstrate that SIF-O_2A retrieved from hyperspectral imagery with a spectral resolution of 0.1 nm FWHM provided a strong explanatory contribution to yield variability (R^2 = 0.66) across the evaluated models. The inclusion of SIF-O_2B in combination with SIF-O_2A resulted in only marginal improvements in model performance (R^2 from 0.66 to 0.67), while models relying solely on SIF-O_2B exhibited inferior performance (R^2 = 0.52) compared to SIF-O_2A derived from both high- and mid-resolution imagery. These findings highlight the sensitivity of SIF-O_2A to photosynthetic activity and its suitability for yield assessment in almond orchards.

Despite these promising results, SIF retrieval remains sensitive to plant stress and environmental conditions. Future work should therefore investigate the effects of stress and variability in environmental conditions, such as changes in VPD, on SIF based yield modelling to assess robustness and operational applicability further.

References

Baker, N.R., 2008: Chlorophyll Fluorescence: A Probe of Photosynthesis In Vivo. *Annual Review of Plant Biology* 59(1), 89–113. doi.org/10.1146/annurev.arplant.59.032607.092759.

Bellvert, J., Adeline, K., Baram, S., Pierce, L., Sanden, B.L., Smart, D.R., 2018: Monitoring Crop Evapotranspiration and Crop Coefficients over an Almond and Pistachio Orchard Throughout Remote Sensing. *Remote Sensing* 10(12), doi.org/10.3390/rs10122001.

Belwalkar, A., Poblete, T., Hornero, A., Hernández-Clemente, R., Zarco–Tejada, P.J., 2024: Improving the Accuracy of SIF Quantified from Moderate Spectral Resolution Airborne Hyperspectral Imager Using SCOPE: Assessment with Sub-Nanometer Imagery. *International Journal of Applied Earth Observation and Geoinformation* 134. doi.org/10.1016/j.jag.2024.104198.

Belwalkar, A., Poblete, T., Longmire, A., Hornero, A., Hernandez-Clemente, R., Zarco-Tejada, P.J., 2022: Evaluation of SIF Retrievals from Narrow-Band and Sub-Nanometer Airborne Hyperspectral Imagers Flown in Tandem: Modelling and Validation in the Context of Plant Phenotyping. *Remote Sensing of Environment* 273. doi.org/10.1016/j.rse.2022.112986.

Calderón, R., Navas-Cortés, J.A., Lucena, C., Zarco-Tejada, P.J., 2013: High-Resolution Airborne Hyperspectral and Thermal Imagery for Early Detection of Verticillium Wilt of Olive Using Fluorescence, Temperature and Narrow-Band Spectral Indices. *Remote Sensing of Environment* 139, 231–245. doi.og/10.1016/j.rse.2013.07.031.

Damm, A., Elber, J., Erler, A., Gioli, B., Hamdi, K., Hutjes, R., Kosvancova, M., Meroni, M., Miglietta, F., Moersch, A., Moreno, J., Schickling, A., Sonnenschein, R., Udelhoven, T., van der Linden, S., Hostert, P., Rascher, U., 2010: Remote Sensing of Sun-Induced Fluorescence to Improve Modeling of Diurnal Courses of Gross Primary Production (GPP). *Global Change Biology* 16(1), 171–186. doi.org/10.1111/j.1365-2486.2009.01908.x.

Gonzalez-Dugo, V., Lopez-Lopez, M., Espadafor, M., Orgaz, F., Testi, L., Zarco-Tejada, P.J., Lorite, I.J., Fereres, E., 2019: Transpiration from Canopy Temperature: Implications for the Assessment of Crop Yield in Almond Orchards. *European Journal of Agronomy* 105, 78–85. doi.org/10.1016/j.eja.2019.01.010.

Government of South Australia, 2026. LocationSAMapViewer. https://location.sa.gov.au/viewer/.

Huang, Y., Xiao, J., Li, X., Xu, Z., Tian, P., Xie, S., Zhang, Z., Zhang, S., Chen, M., Chen, Y., 2025: High Temperature and VPD Amplify Tidal Suppression of the SIF–GPP Relationship in a Mangrove Restoration Area in Southeast China. *IEEE Transactions on Geoscience and Remote Sensing* 63. doi.org/10.1109/TGRS.2025.3608266.

Idso, S. B., Jackson, R.D., Pinter,P.J., Reginato,R.J., Hatfield, J. L., 1981: Normalizing the Stress-Degree-Day Parameter for Environmental Variability. *Agricultural Meteorology* 24, 45–55. doi.org/10.1016/0002-1571(81)90032-7.

Maier, S.W., Günther, K.P., Stellmes, M., 2004: *Sun-Induced Fluorescence: A New Tool for Precision Farming*. *Digital Imaging and Spectral Techniques: Applications to Precision Agriculture* 66, 207 - 222.

Meroni, M., Rossini, M., Guanter, L., Alonso, L., Rascher, U., Colombo, R., Moreno, J., 2009: Remote Sensing of Solar-Induced Chlorophyll Fluorescence: Review of Methods and Applications. *Remote Sensing of Environment* 113(10), 2037–2051. doi.org/10.1016/j.rse.2009.05.003.

Silvani, D., Dymaxion Labs, 2019. Zonal Statistics for Multiband Rasters – QGIS plugin. https://github.com/dymaxionlabs/qgis-zonal-statistics-multiband/commits/master/ (15 May 2026).

Tang, M., Sadowski, D.L., Peng,C., Vougioukas, S.G., Klever, B., Khalsa, S.D.S., Brown, P.H., Jin,Y., 2023: Tree-Level Almond Yield Estimation from High Resolution Aerial Imagery with Convolutional Neural Network. *Frontiers in Plant Science* 14. doi.org/10.3389/fpls.2023.1070699.

Verrelst, J., van der Tol, C., Magnani, F., Sabater, N., Rivera, J.P., Mohammed, G., Moreno, J., 2016: Evaluating the predictive power of sun-induced chlorophyll fluorescence to estimate net photosynthesis of vegetation canopies: A SCOPE modeling study. *Remote Sensing of Environment* 176, 139 – 151. doi.org/10.1016/j.rse.2016.01.018

Wang, Y., Suarez, L., Poblete, T., Gonzalez-Dugo, V., Ryu, D., Zarco-Tejada,P.J., 2022: Evaluating the Role of Solar-Induced Fluorescence (SIF) and Plant Physiological Traits for Leaf Nitrogen Assessment in Almond Using Airborne Hyperspectral Imagery. *Remote Sensing of Environment* 279. doi.org/10.1016/j.rse.2022.113141.